

# Supplemental Material:

## Unconventional field-induced spin gap in an $S = 1/2$ chiral staggered chain

J. Liu,<sup>1</sup> S. Kittaka,<sup>2</sup> R. D. Johnson,<sup>1</sup> T. Lancaster,<sup>3</sup> J. Singleton,<sup>4</sup> T. Sakakibara,<sup>2</sup> Y. Kohama,<sup>2</sup> J. van Tol,<sup>5</sup> A. Ardavan,<sup>1</sup> B. H. Williams,<sup>1</sup> S. J. Blundell,<sup>1</sup> J. L. Manson,<sup>6,\*</sup> and P. A. Goddard<sup>7,†</sup>

<sup>1</sup>*Department of Physics, Clarendon Laboratory, University of Oxford, Parks Road, Oxford OX1 3PU, UK*

<sup>2</sup>*Institute for Solid State Physics, University of Tokyo, Kashiwa, Chiba 277-8581, Japan*

<sup>3</sup>*Centre for Materials Physics, Durham University, South Road, Durham DH1 3LE, UK*

<sup>4</sup>*National High Magnetic Field Laboratory, Los Alamos National Laboratory, MS-E536, Los Alamos, NM 87545, USA*

<sup>5</sup>*National High Magnetic Field Laboratory, Florida State University, Tallahassee, Florida 32310, USA*

<sup>6</sup>*Department of Chemistry and Biochemistry, Eastern Washington University, Cheney, WA 99004, USA*

<sup>7</sup>*Department of Physics, University of Warwick, Gibbet Hill Road, Coventry, CV4 7AL, UK*

### I. SAMPLES

Crystals of  $[\text{Cu}(\text{pym})(\text{H}_2\text{O})_4][\text{SiF}_6]\text{H}_2\text{O}$  grow as rod-like blocks with the long axis of the crystal parallel to the Cu—pym chain. For the heat capacity measurements a sample of dimensions  $7 \times 2 \times 1 \text{ mm}^3$  was used. For susceptibility measurements the sample was  $6 \times 1.5 \times 1.5 \text{ mm}^3$ . The ESR measurements made use of crystals with similar aspect ratios. For the room-temperature measurements the sample length was 1.5 mm and for the low-temperature ESR data the sample was 2 mm long.

### II. MUON-SPIN RELAXATION

Zero field (ZF) muon-spin relaxation ( $\mu^+\text{SR}$ ) measurements were made at the ISIS Facility, Rutherford Appleton Laboratory, UK using the EMU instrument and at the Swiss Muon Source, Paul Scherrer Institut, CH using the LTF instrument. The polycrystalline sample was mounted on a silver plate using a thin layer of silicon grease. In a  $\mu^+\text{SR}$  experiment [S1] spin-polarized positive muons are stopped in a target sample, where the muon usually occupies an interstitial position in the crystal. The observed property in the experiment is the time evolution of the muon spin polarization, the behaviour of which depends on the local magnetic field  $B$  at the muon site. Each muon decays, with a lifetime of  $2.2 \mu\text{s}$ , into two neutrinos and a positron, the latter particle being emitted preferentially along the instantaneous direction of the muon spin. Recording the time dependence of the positron emission directions therefore allows the determination of the spin-polarization of the ensemble of muons. In our experiments positrons are detected by detectors placed forward (F) and backward (B) of the initial muon polarization direction. Histograms  $N_F(t)$  and  $N_B(t)$  record the number of positrons detected in the two detectors as a function of time  $t$  following the muon implantation. The quantity of interest is the decay positron asymmetry function, defined as

$$A(t) = \frac{N_F(t) - \alpha_{\text{exp}} N_B(t)}{N_F(t) + \alpha_{\text{exp}} N_B(t)}, \quad (\text{S1})$$

where  $\alpha_{\text{exp}}$  is an experimental calibration constant.  $A(t)$  is proportional to the spin polarization of the muon ensemble.

The ZF spectrum measured at 20 mK is shown in Fig. S1. We note that no oscillations or related signatures are observed in the muon asymmetry, which strongly suggests that the material does not magnetically order at temperatures above 20 mK. The measured spectra are found to contain two contributions. The first is a fast relaxing component  $A_1$  which dominates the signal at early times and is well described by an exponential function  $\exp(-\lambda t)$ . The second is a larger, slowly relaxing component  $A_2$ , which dominates at intermediate times and fits to the Kubo-Toyabe (KT) function  $f_{\text{KT}}(\Delta, B_{\text{app}}, t)$  [S2] where  $\Delta$  is the second moment of the static, local magnetic field distribution defined by  $\Delta = \gamma_\mu \sqrt{\langle (B - \langle B \rangle)^2 \rangle}$ ,  $B_{\text{app}}$  is the magnitude of the applied longitudinal magnetic field and  $\gamma_\mu (= 2\pi \times 135.5 \text{ MHz T}^{-1})$  is the muon gyromagnetic ratio. The KT function is characteristic of spin relaxation due to a random, quasi-static distribution of local magnetic fields at diamagnetic muon sites. We do not observe the recovery in asymmetry at late times that is expected for the static KT function. The lack of this recovery is probably due to

---

\* [jmanson@ewu.edu](mailto:jmanson@ewu.edu)

† [p.goddard@warwick.ac.uk](mailto:p.goddard@warwick.ac.uk)

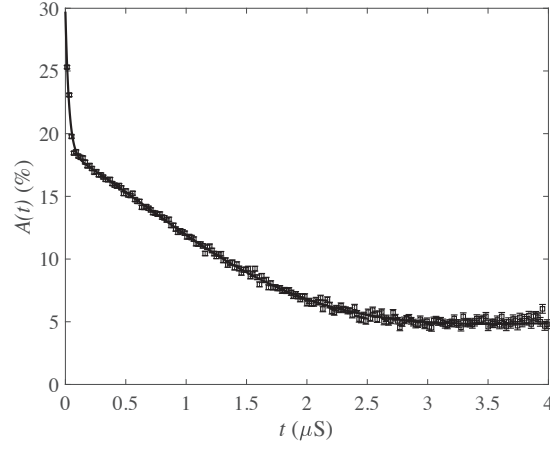


FIG. S1. (a) ZF  $\mu^+$ SR spectrum measured at 20 mK showing a contribution from two components. A fit is shown to Eq. (S2).

slow dynamics in the random field distribution and is crudely modelled here with an exponential term  $\exp(-\Lambda t)$ . The data were found to be best fitted with the resulting function over the entire time range

$$A(t) = A_1 f_{\text{KT}}(\Delta, B_{\text{app}}, t) \exp(-\Lambda t) + A_2 \exp(-\lambda t) + A_{\text{bg}} \quad (\text{S2})$$

where  $A_{\text{bg}}$  represents a constant background signal from those muons that stop in the sample holder. The fitted magnitude of  $\Delta \approx 0.5$  MHz suggests that the random magnetic field distribution giving rise to the KT function is due to nuclear magnetic moments, implying that the field due to electronic moments at these muon sites is motionally narrowed out of the spectrum due to very rapid fluctuations. The observation of two distinct components,  $A_1$  and  $A_2$ , in the asymmetry spectrum suggests that there are two distinct muon stopping states in the material. We note that behaviour consistent with two muon sites has been observed previously in copper chain compounds with similar structures.

From the observation that the material does not undergo a magnetic ordering transition above 20 mK, it is possible to put an upper limit on any interchain interaction present in the system. The onset temperature of long-range order in highly one-dimensional  $S = 1/2$  antiferromagnets depends critically on the ratio of the interchain ( $J_{\perp}$ ) to intrachain ( $J$ ) exchange strengths [S3]. Using the relation given in that reference, the lack of long-range order indicates that  $J_{\perp}/J < 1.7 \times 10^{-4}$  or  $J_{\perp} < 7$  mK.

### III. CRYSTAL SYMMETRY AND DZHALOSHINSKII-MORIYA INTERACTIONS

As for all exchange interactions present in the spin Hamiltonian, in the absence of symmetry-breaking order or external fields, the antisymmetric Dzyaloshinskii-Moriya (DM) interaction must respect the symmetry of the parent crystal structure. The relevant term in the mean-field energy is typically written  $\mathbf{D} \cdot (\hat{\mathbf{S}}_i \times \hat{\mathbf{S}}_j)$ , where the DM interaction is represented by a time-even and parity-even pseudo vector (axial vector),  $\mathbf{D}$ .

The crystal structure of  $[\text{Cu}(\text{pym})(\text{OH}_2)_4][\text{SiF}_6]\text{H}_2\text{O}$  has space group  $P4_12_12$ , and is composed of two chiral Cu(pyrimidine) chains per unit cell with a common, global chirality. The two chiral chains are related by the  $2_1$  and  $2$  symmetry operators of the space group (note that both  $2_1$  and  $2$  operations do not switch structural chirality, which is formally represented by a time-even, parity-odd pseudo scalar). An individual chain has symmetry  $4_1$ , such that 4 Cu atoms bonded together via pyrimidine molecules complete a full chiral rotation per unit cell. When occurring by itself,  $4_1$  symmetry supports a uniform  $\mathbf{D}_u$  parallel to the axis of the chain. The  $4_1$  symmetry also supports a four-fold staggered  $\mathbf{D}_s$  lying perpendicular to the uniform  $\mathbf{D}_u$ , which transforms in the same way as the Cu-(pyrimidine)-Cu bonds.

Without loss of generality, the DM interaction in  $[\text{Cu}(\text{pym})(\text{OH}_2)_4][\text{SiF}_6]\text{H}_2\text{O}$  can be decomposed into the two orthogonal components, uniform and staggered, described above. We note, however, that the two terms in the mean-field energy will have common components of the spins, such that they cannot be minimised independently.

Finally, we note that space group  $P4_12_12$  does not support a net  $\mathbf{D}$ . The  $2_1$  and  $2$  symmetry operators give the same configuration of staggered  $\mathbf{D}_s$  on every chain, but opposite signs of the uniform  $\mathbf{D}_u$  for the two chiral chains in each unit cell.

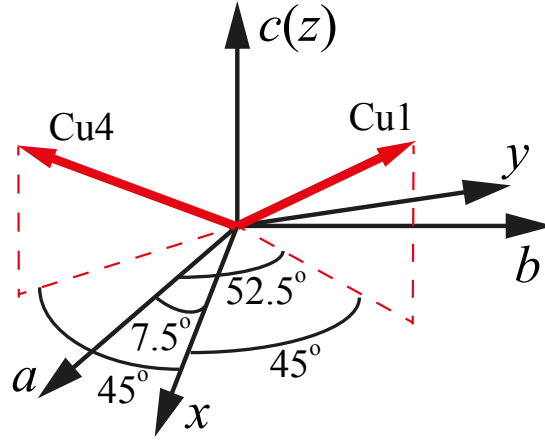


FIG. S2. Schematic plot showing the relationship between the crystalline  $abc$  axes and the laboratory frame  $xyz$ . The red arrows represents the JT axes of Cu1 and Cu4, i.e. the local principal  $g$  axes, and the dashed lines indicate their projection into the  $ab$  plane. The projection of the JT axis for Cu1 is  $52.5^\circ$  away from the  $a$  axis. The  $x$  axis lies halfway between the projections of the JT axes for Cu1 and Cu4, making it  $7.5^\circ$  away from the  $a$  axis.

#### IV. ELECTRON SPIN RESONANCE

##### IV.a. Room-temperature electron spin resonance and staggered $g$ tensors

In order to separate the uniform and staggered parts of the  $g$  tensors, it is convenient to define a laboratory frame  $xyz$  based on the Jahn-Teller (JT) axes of the Cu(II) atoms. This  $xyz$  coordination is chosen such that the  $g$  tensors for each  $\text{Cu}^{2+}$  spins can be separated into a uniform diagonal part, invariant for all spins, and staggered off-diagonal parts. To achieve this, the  $x$  axis is set to be midway between the projections of two adjacent JT axes in the  $ab$  plane. Therefore, the  $x$  axis lies within the  $ab$ -plane and it is rotated  $7.5^\circ$  away from the  $a$  axis. The  $z$  axis is parallel to the crystallographic  $c$  axis. The conversion between the crystalline  $abc$  axes and the  $xyz$  frame is shown in Fig. S2.

An anisotropic  $g$  tensor is expected for the Cu(II) spins due to the JT distorted octahedral coordination environment surrounding the Cu(II) ions. The JT axis, defined as the elongated Cu—O bond, lies  $9.1^\circ$  out of the  $xy$  plane. The local principal axis of the  $g$  tensor is expected to be parallel to the JT axis. Assuming tetragonal local symmetry, the local  $g$  tensor is expected to take the diagonalized form:

$$g_{\text{loc}} = \begin{pmatrix} g_{\perp} & 0 & 0 \\ 0 & g_{\perp} & 0 \\ 0 & 0 & g_{\parallel} \end{pmatrix} \quad (\text{S3})$$

with the  $g_{\parallel}$  component along the elongated JT axis ( $g_{\parallel} > g_{\perp}$ ). The local  $g$  tensors for individual spins can be transformed to the global  $xyz$  coordination with the following Euler rotations:

$$g_i^{xyz} = Q_i^T g_{\text{loc}} Q_i \quad (\text{S4})$$

with

$$Q_i = \begin{pmatrix} 1 & 0 & 0 \\ 0 & \cos \theta & \sin \theta \\ 0 & -\sin \theta & \cos \theta \end{pmatrix} \begin{pmatrix} \cos \phi_i & \sin \phi_i & 0 \\ -\sin \phi_i & \cos \phi_i & 0 \\ 0 & 0 & 1 \end{pmatrix} \quad (\text{S5})$$

$\theta = 80.9^\circ (90 - 9.1)$ , which is the tilting angle between the JT axis and the  $z$  axis.  $\phi_i = 45^\circ, 135^\circ, 225^\circ$  and  $315^\circ$  for  $i = 1, 2, 3$  and  $4$ , respectively, in consistent with the four-fold rotation of the local coordination environment about the  $z$  axis. In the strong coupling limit, the average of the four Cu(II) sites within a unit cell give the  $g$  values observed in ESR measurements [Fig. 2(a) in the main text]:

$$\frac{1}{4} \sum_{i=1}^4 g_i^{xyz} = \begin{pmatrix} 2.21 & 0 & 0 \\ 0 & 2.21 & 0 \\ 0 & 0 & 2.10 \end{pmatrix} \quad (\text{S6})$$

By combining Eq. S3-S6, we obtained  $g_{\parallel} = 2.33$  and  $g_{\perp} = 2.09$ . Therefore, according to Eq. S4, the  $g$  tensors for individual spins in the  $xyz$  coordination frame is:

$$\begin{aligned} g_1^{xyz} &= \begin{pmatrix} 2.210 & -0.12 & 0.026 \\ -0.12 & 2.21 & -0.026 \\ 0.026 & -0.026 & 2.10 \end{pmatrix} & g_2^{xyz} &= \begin{pmatrix} 2.210 & 0.12 & 0.026 \\ 0.12 & 2.21 & 0.026 \\ 0.026 & 0.026 & 2.10 \end{pmatrix} \\ g_3^{xyz} &= \begin{pmatrix} 2.210 & -0.12 & -0.026 \\ -0.12 & 2.21 & 0.026 \\ -0.026 & 0.026 & 2.10 \end{pmatrix} & g_4^{xyz} &= \begin{pmatrix} 2.210 & 0.12 & -0.026 \\ 0.12 & 2.21 & -0.026 \\ -0.026 & -0.026 & 2.10 \end{pmatrix} \end{aligned} \quad (S7)$$

Which corresponds to Eq. 1 in the main text. When a transverse field is applied parallel to the  $x$  axis,  $\mathbf{H}_0 = [H_0, 0, 0]$ , the effective fields ( $\mathbf{H}_i$ ) on the  $i$ th Cu site is:

$$\mathbf{H}_1 = \begin{pmatrix} 2.21H_0 \\ -0.12H_0 \\ 0.026H_0 \end{pmatrix}, \mathbf{H}_2 = \begin{pmatrix} 2.21H_0 \\ 0.12H_0 \\ 0.026H_0 \end{pmatrix}, \mathbf{H}_3 = \begin{pmatrix} 2.21H_0 \\ -0.12H_0 \\ -0.026H_0 \end{pmatrix}, \mathbf{H}_4 = \begin{pmatrix} 2.21H_0 \\ 0.12H_0 \\ -0.026H_0 \end{pmatrix} \quad (S8)$$

Eq. S8 is the field configuration in Fig. 3(b) of the main text. The two-fold staggered fields are in the  $y$  direction while the four-fold staggered fields lies parallel to the  $z$  axis.

The room-temperature ESR resonance has the Lorentzian shape expected for an exchange-coupled system. The linewidth ( $\Delta H$ ) [Fig. 2(b) in the main text] has a strong angular dependence, probably due to the staggered  $g$  tensors as well as DM interactions [S4–S6]. In the high temperature limit ( $k_B T \gg J$ ), when the isotropic exchange interactions is large compared to the ESR linewidth ( $J \gg g\mu_B \Delta H$ ), the ESR resonance is expected to have Lorentzian profile with a linewidth [S4]:

$$\Delta H = \frac{2\pi}{\sqrt{6}} \frac{k_B}{g\mu_B} \left( \frac{M_2^3}{M_4} \right)^{1/2}, \quad (S9)$$

$M_2$  and  $M_4$  are the second and fourth moment of the resonance and their explicit expressions can be found in Ref. [S4].

The wide ESR resonance suggests the existence of sizable DM interactions. However, we found it is difficult to reproduce the extreme orientation dependence of  $\Delta H$ , which varies between 50–550 mT. For instance, with  $D_u = 1.5$  K,  $\Delta H = 50$  mT for  $H$  perpendicular to the  $c$  axis. Such a value of  $D_u$  is reasonable as the magnitude of the DM interaction is expected to be proportional to  $J \times \delta g/g$ , where  $\delta g$  is the anisotropy in  $g$ . On the other hand, this  $D_u$  would lead to  $\Delta H = 75$  mT for  $H \parallel c$ , which is significantly smaller than the experimental result. Furthermore, we found it is impossible to simulate the angular dependence solely based on Eq. S9 with any combination of  $D_u$  and  $D_s$ . This suggests additional broadening effects need to be considered to explain the result. One possible candidate is spin diffusion due direct flip-flop processes [S7, S8]. These energy-conserving processes are maximal for  $H \parallel c$  such that all spins have the same resonance frequency, leading to extra broadening of the ESR signal. When the field is rotated away from the  $c$ -axis, the resonance frequencies of the neighboring spin centers differ, suppressing the extra broadening effect.

#### IV.b. Low-temperature ESR results

The low-temperature multiple frequency ESR measurements were performed with a transmission type ESR spectrometer using a millimeter vector network analyzer as the microwave source and detector. The experiments were performed with the applied field perpendicular to the crystal  $c$  axis. For a given frequency, the spectrum can be divided into the low-field and high-field regimes, as depicted by the dashed line in Fig. S3(a). In the high-field side of the spectra, six strong resonances can be resolved and followed through the experimental frequency range. As we discussed in the main text, these six resonances are reminiscent of the breather excitations observed in  $[\text{pym-Cu}(\text{NO}_3)_2(\text{H}_2\text{O})_2]$ , albeit only three breather modes were expected for the experimental field range.

One possible reason for the extra high-field resonances in our material is that the unit cell of  $\text{Cu}(\text{pym})(\text{H}_2\text{O})_4[\text{SiF}_6] \cdot \text{H}_2\text{O}$  contains four inequivalent  $\text{Cu}^{2+}$  spins, double that for  $[\text{pym-Cu}(\text{NO}_3)_2(\text{H}_2\text{O})_2]$ , although it is not obvious exactly how the larger unit cell may lead to the additional resonances. Another possible explanation is that the breather modes are affected by a field parallel to the chain axis, e.g. due to a small field misalignment. This longitudinal field causes different effects to the chains with opposite  $\mathbf{D}_u$ . In this case, the signal could be due to two groups of breather excitations, each with three modes as predicted by the SG model, arising due to differences in the effective staggered fields

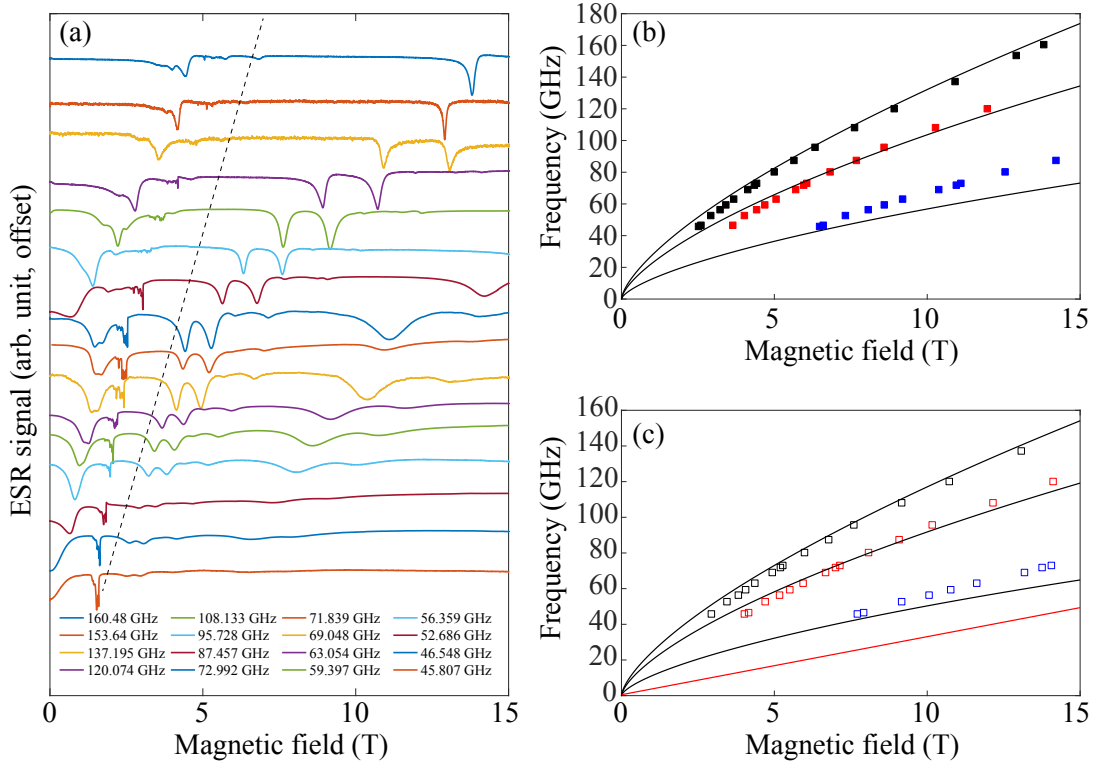


FIG. S3. (a) ESR spectra for  $\text{Cu}(\text{pym})(\text{H}_2\text{O})_4[\text{SiF}_6]\cdot\text{H}_2\text{O}$  recorded at 1.9 K with the field applied perpendicular to the crystalline  $c$ -axis. The spectra are separated into two regimes, the low-field part and the high field part, indicated by the dashed line in (a). (b) and (c) Frequency vs field plot showing the high-field ESR transitions following the label scheme used in Fig. 2(c) in the main text. The solid black lines are the best fit to the data using the sine-Gordon model described in Eq. S10 and S11. The red line shows the linear dependence of the energy gap  $\Delta$  [Fig. 2(f) of the main text] as determined from heat capacity measurements and converted into GHz units. This is everywhere lower than the ESR excitation frequencies, implying that the minimum gap could be at a point in  $k$ -space not probed by ESR.

between the two subspecies with opposite  $\mathbf{D}_u$ . This could also account for the similar amplitudes of the resonances marked by open/filled black squares [see Fig. 2(c) in main text].

To explore this possibility within the existing model of non-chiral chains, attempts were made to fit the high-field ESR resonances with two sets of breathers modes with different parameters. In the SG model, the  $n$ th breather gap is expected to be [S9]:

$$\Delta_n = 2\Delta_s \sin n\pi\xi/2 \quad (\text{S10})$$

where  $\Delta_s$  is the soliton gap

$$\Delta_s = J \frac{2\Gamma(\xi/2)v_F}{\sqrt{\pi}\Gamma[(1+\xi)/2]} \left[ \frac{g\mu_B H}{Jv_F} \frac{\pi\Gamma[1/(1+\xi)]cA_x}{2\Gamma[\xi/(1+\xi)]} \right]^{(1+\xi)/2} \quad (\text{S11})$$

At a given field  $H$ , there are  $n = 1, \dots, [1/\xi]$  breather branches.  $\xi(H/J)$ ,  $v_F(H/J)$  and  $A_x(H/J)$  in Eq. S10 and S11 are known [S10]. The value of  $\xi(H/J)$  varies between 0.3065 and 0.2585 in the experimental field range; hence three branches are expected.  $J$  is the antiferromagnetic interaction between spins and is set to 42.3 K (see main text). The only free parameter in the fitting is the effective staggered field coupling  $c = h_{2s}/H$ , which should be close to  $g_{2s}$ .

The best fits are shown in by the solid lines in Fig. S3(b) and (c). We found it is impossible to simultaneously fit all three branches for either set of resonances. In addition, within each branch, the field dependence of the resonances also deviate from the SG model considerably. Furthermore, the fits gives the  $c$  value of 0.011 and 0.013, significantly smaller than the measured  $g_{2s}$ . Therefore, we conclude it is impossible to model the low-temperature ESR spectra with the SG model proposed for the two-fold staggered chains [S9, S10].

Analyzing the low-field transitions in Fig. S3(a) is challenging due to the difficulty in classifying the resonances within the experimental frequency/field range. In most spectra, a relatively broad peak is observed at low fields end

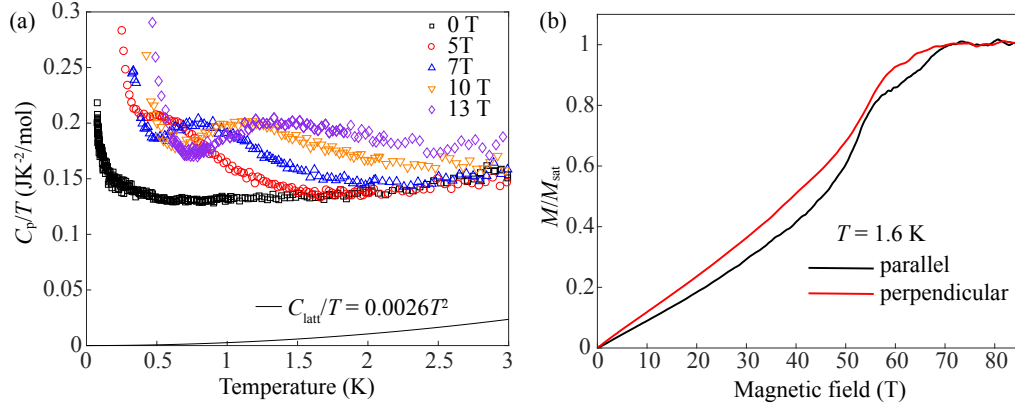


FIG. S4. (a) Temperature dependence of the heat capacity,  $C_p$ , in different transverse fields ( $H \perp c$ ). A broad peak was observed around 0.52, 0.81, 1.1 and 1.3 K for  $H = 5, 7, 10$  and  $13$  T, respectively. The solid line is the calculated lattice contribution. (b) Magnetization of  $[\text{Cu}(\text{pym})(\text{H}_2\text{O})_4]\text{SiF}_6 \cdot \text{H}_2\text{O}$  divided by the saturation magnetization  $M_{\text{sat}}$  taken using pulsed magnetic fields at 1.6 K. The field is applied both parallel (black line) and perpendicular (red line) to the chain axis. The saturation field is consistent with the value of the intrachain exchange constant as determined from both heat capacity and low-field magnetic susceptibility.

with a fine structure. As shown in Fig. 2(c) in the main text, upon cooling, the paramagnetic resonance shifts towards lower field and eventually splits into two peaks. A similar low-temperature evolution of the ESR spectra has been reported in  $\text{Cs}_2\text{CuCl}_4$  and  $\text{K}_2\text{CuSO}_4\text{Br}_2$ , which is attributed to the splitting of the spinon continuum around  $k = 0$  when the magnetic field has a component along the DM interaction [S11, S12]. However, the four-fold staggered  $\mathbf{D}_S$  configuration makes it impossible for the field to be either parallel or perpendicular to all DM vectors, complicating the ESR spectra. On the other hand, it is challenging to identify the other sharp resonances observed in the low-field part of the spectra. Similar resonances were observed in the ESR study for  $[\text{pym}-\text{Cu}(\text{NO}_3)_2(\text{H}_2\text{O})_2]$  and were speculated to be related to chain-edge effects [S9, S13].

## V. HEAT CAPACITY

### V.a. Subtraction of nuclear Schottky anomaly.

The heat capacity ( $C_p$ ) was measured as a function of temperature and magnetic field. In order to minimize the contribution from nuclear spins at low temperatures, the measurement was performed with a deuterated sample,  $[\text{Cu}(\text{pym-D})(\text{D}_2\text{O})_4]\text{SiF}_6 \cdot \text{D}_2\text{O}$ . Fig. S4(a) shows  $C_p/T$  recorded with the field applied perpendicular to the crystalline  $c$  axis. At zero field, for  $T > 0.8$  K,  $C_p$  can be well described with  $C_p = \alpha T + \beta T^3$ , where the first and second terms correspond to the 1D spin correlation and the lattice contribution, respectively. Fitting the zero-field data gives  $C_{\text{latt}} = \beta T^3$  with  $\beta = 2.6$  mJ/(mol K<sup>4</sup>). This  $C_{\text{latt}}$  contribution is independent of the applied field and is removed from all data.

Upon cooling the sample,  $C_p$  exhibits a board peak when an external field is applied before a sharp upturn at the lowest temperatures. Similar behavior was observed in the hydrogenated sample. The broad peak is related to the field induced gap discussed in the main text. On the other hand, We found the low temperature upturns the can be described as  $C_p \propto T^{-2}$  and is likely due to a nuclear Schottky effect [S14]. The nuclear heat capacity  $C_n$  is expected to follow  $C_n = (a_0 + a_1 H^2)/T^2$ .  $a_0$  is due to nuclear quadrupole splitting of nuclei with nuclear spins  $I > 1/2$  while  $a_1$  is the nuclear Zeeman energy.

At zero field, the  $\mu^+\text{SR}$  data shown no evidence of magnetic order above 20 mK and no spin gap is expected for a  $S = 1/2$  AFM chain. Therefore, below 0.2 K, the zero-field heat capacity data is fitted with  $C_p = a_0 T^{-2} + \alpha T$ , yielding  $a_0 = 27 \mu\text{J K/mol}$ . The  $a_0$  value is then fixed with the  $a_1$  as the only variable in fitting the low-temperature  $C_p$  data with a nonzero field. We found the data can be well fitted with  $a_1 = 123 \mu\text{J K/(mol T}^2)$ , giving  $C_n = (27 + 123 H^2)/T^2 \mu\text{J/(mol K)}$ . This nuclear heat capacity was subtracted from all  $C_p$  data measured with the application of a magnetic field [Fig. 2(f) in the main text].

We note the coefficient  $a_1$  is larger than expected from the nominal composition of the sample. In principle, the Zeeman energy contribution to the heat capacity can be calculated as  $a_1 = \sum n_I \hbar^2 \gamma_I^2 I(I+1)/3k_B$ . The summation is over all atoms in the chemical formula with a nuclear spin  $I \neq 0$ .  $n_I$  is the number of the nuclei per mole,  $\hbar$  is



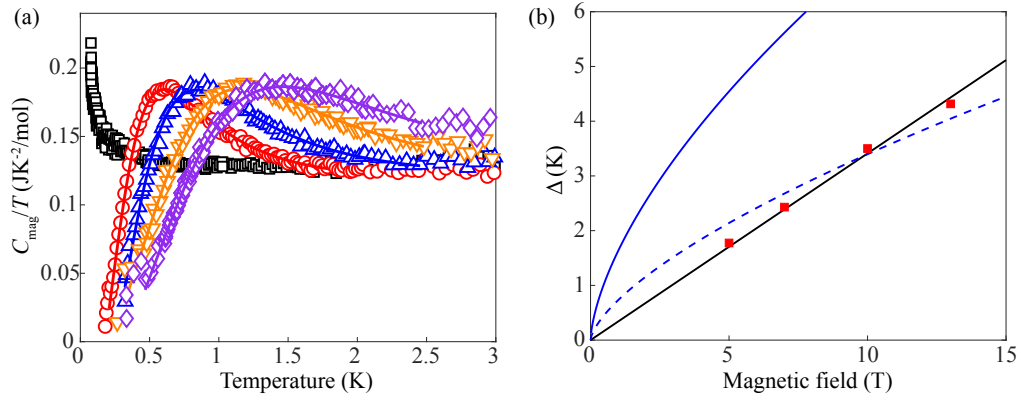


FIG. S5. (a) Result of fitting the simple two-level model (lines) described below to experimental  $C_{\text{mag}}/T$  data (points). (b) Field dependence of the gap (squares) deduced from the fits in (a), as well as a best fit to a linear model (black line), a best fit to the SG model (dotted blue line), and the size of the gap predicted by the SG model using the experimentally-determined value of the two-fold staggered field (solid blue line).

the Planck constant,  $\gamma_I$  is the gyromagnetic ratio, and  $k_B$  is the Boltzmann constant. Based on the nominal chemical formula of the deuterated sample, one would expect  $a_1 = 57 \mu\text{J K}/(\text{mol T}^2)$ . Indeed, we found the fitted value of  $a_1 = 123 \mu\text{J K}/(\text{mol T}^2)$  would correspond to a H:D ratio close to 8:6, rather than all 14 H atoms are replaced by D. We suspect this is due to partially rehydrogenation whereby  $\text{H}_2\text{O}$  replaces some of the  $\text{D}_2\text{O}$  during the crystal growth, leading to the discrepancy between the nominal and experimental determined  $a_1$  values.

### V.b. Fitting to obtain the gap size.

The temperature-dependence of the heat capacity of a gapped system will have a broad Schottky-like hump whose shape and position depends on the size of the gap and the degeneracy and distribution of excited states averaged across the Brillouin zone. In the manuscript the magnetic heat capacity is fitted with a model derived from the SG theory. While we stress that the SG model is not adequate to quantitatively account for many features of our data, there are still strong similarities between our system and that of the SG materials, particularly the staggered  $g$ -tensors and the richness of the excitation spectrum observed by ESR. Therefore the best possible expression that currently exists to reliably estimate the size of the gap from the heat capacity of our system is that derived from the SG model.

Nevertheless, in order to show that the linear field dependence of the gap is not an artefact of using the SG heat-capacity expression, we also fit our data at fixed fields to a model consisting of a two-level system (Schottky anomaly) plus a constant  $C/T$  term that accounts for the Tomonaga-Luttinger liquid behaviour observed at high temperatures. This is certainly not the ideal model to use to extract a reliable estimate of absolute size of the gap. This is because, while the heat capacity will be strongly influenced by the gap between the ground state and lowest energy excited state, any higher energy states will also have a significant effect. Such higher energy states are observed in the ESR spectra, but are not taken into account in this simple model. Thus we would expect the absolute size of the gap extracted in this way to be an overestimate.

This is what we observe in Fig. S5: panel (a) shows the result of fitting this two-level model to our data and it is seen that the form of the data is reasonably well-described by the model. The points in panel (b) shows the size of the gap and its evolution in field. This procedure illustrates several issues: (i) the form of the heat capacity data are well described by a generic gapped model; (ii) the size of the gap extracted using this model, which is expected to be a overestimate of the actual gap, is still smaller across the measured field range than that predicted by the SG model using the experimentally-determined size of the two-fold staggered field in our material (solid blue line); and (iii) the gap thus extracted has a linear field-dependence (black line) and cannot be described by the SG model even with a staggered field much smaller than that measured (dotted blue line).

## VI. PULSED-FIELD MAGNETIZATION

Pulsed-field magnetization experiments used a compensated-coil susceptometry technique, described in [S15]. Fields were provided by the 65 T short-pulse and 100 T multi-shot magnets at NHMFL, Los Alamos. The susceptometer

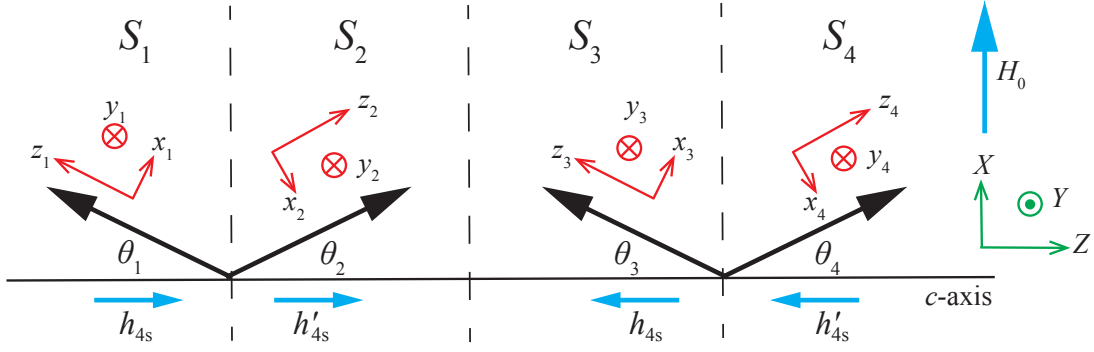


FIG. S6. Schematic figure showing the  $XZ$  canted ground state and the staggered fields for  $[\text{Cu}(\text{pym})(\text{H}_2\text{O})_4]\text{SiF}_6 \cdot \text{H}_2\text{O}$ . The plot shows the crystallographic unit cell of  $\text{Cu}(\text{pym})$ , which includes four spins named as  $S_1 \sim S_4$ . The black arrows represents the spins for  $\text{Cu}(\text{II})$  while the cyan arrows illustrating the arrangement of the staggered fields. The global and local coordination systems are labelled by green and red colours, respectively.

was placed within a  $^4\text{He}$  cryostat providing temperatures down to 1.6 K. Magnetic field was measured by integrating the voltage induced in a ten-turn coil calibrated by observing the de Haas-van Alphen oscillations of the belly orbits of the copper coils of the susceptometer. To create the traces shown in Fig. S4(b), data below 65 T taken using the 65 T short pulse magnet were combined with data above 40 T taken using the 100 T multi-shot magnet. Both experiments made use of the same sample and susceptometer.

## VII. SPIN-WAVE EXPANSION

We present a calculation for the excitation gap based on the standard spin-wave approximation for the  $XZ$  canted structure with four-fold staggered fields  $h_{4s}$  and  $h'_{4s}$ . In the following calculation, we define the  $XYZ$  frame as the laboratory frame. The  $c$  axis of the chain is parallel to  $Z$  and a external field  $H_0$  is applied in the  $X$  direction. The  $x_i y_i z_i$  frames represent the local coordination systems for the  $i$ th  $\text{Cu}^{2+}$  ion where  $z_i$  axes are defined by the direction of the  $i$ th spin (Fig. S6). With an external field applied perpendicular to the chain, the four-fold staggered fields are parallel to the chain propagation direction ( $c$ -axis). This is the situation illustrated in Fig. S6 (also see Fig. 3(b) in the main text). The magnitudes of staggered fields,  $h_{4s}$  and  $h'_{4s}$ , depend on the explicit form of the staggered  $g_{\text{methr}m4s}$  and can be treated as twin independent parameters. However, as long as the field is applied within the  $XY$  plane, the resultant four-fold staggered field should always be parallel to the  $Z$  axis. The canted antiferromagnetic configuration of the spins, as well as the polarities of stagger fields, are illustrated in Fig. S6. The canted angles,  $\theta_n$  ( $n = 1$  to 4), are determined by both the external field  $H_0$  and the staggered fields. Therefore, Eq. 3 in the main text does not hold rigorously due to the possibility that  $\theta_1 \neq \theta_2 \neq \theta_3 \neq \theta_4$ . The energy per unit cell of the canted antiferromagnet state is:

$$\begin{aligned}
 E = & -JS^2[\cos(\theta_1 + \theta_2) + \cos(\theta_2 + \theta_3) + \cos(\theta_3 + \theta_4) + \cos(\theta_4 + \theta_1)] \\
 & -H_0S[\sin\theta_1 + \sin\theta_2 + \sin\theta_3 + \sin\theta_4] \\
 & +h_{4s}S(\cos\theta_1 - \cos\theta_3) - h'_{4s}S(\cos\theta_2 - \cos\theta_4)
 \end{aligned} \tag{S12}$$

This energy is minimized for  $\partial E / \partial \theta_n = 0$ , which gives:

$$\begin{aligned}
 \frac{\partial E}{\partial \theta_1} &= JS^2[\sin(\theta_1 + \theta_2) + \sin(\theta_1 + \theta_2)] - H_0S \cos\theta_1 - h_{4s}S \sin\theta_1 = 0 \\
 \frac{\partial E}{\partial \theta_2} &= JS^2[\sin(\theta_1 + \theta_2) + \sin(\theta_2 + \theta_3)] - H_0S \cos\theta_2 + h'_{4s}S \sin\theta_2 = 0 \\
 \frac{\partial E}{\partial \theta_3} &= JS^2[\sin(\theta_2 + \theta_3) + \sin(\theta_3 + \theta_4)] - H_0S \cos\theta_3 + h_{4s}S \sin\theta_3 = 0 \\
 \frac{\partial E}{\partial \theta_4} &= JS^2[\sin(\theta_3 + \theta_4) + \sin(\theta_4 + \theta_1)] - H_0S \cos\theta_4 - h'_{4s}S \sin\theta_4 = 0
 \end{aligned} \tag{S13}$$

The staggered fields,  $h_{4s}$  and  $h'_{4s}$ , are much smaller than  $H_0$ . The canted angles,  $\theta_n$ , are mostly determined by  $H_0$  while the staggered fields lead to a small correction to  $\theta_n$ . Therefore, the canted angles can be written as  $\theta_n = \theta + \delta\theta_n$



where  $\theta = \arcsin(H_0/4JS)$  is the canted angle induced by  $H_0$ .  $\delta\theta_n$ 's are the small corrections caused by the staggered fields and  $\theta \gg \theta_n$ . Hence, Eq. S13 can be written as:

$$\begin{aligned} 16J^2S^2\delta\theta_1 + (8J^2S^2 - H^2)(\delta\theta_2 + \delta\theta_4) &= 2h_{4s}H_0 \\ 16J^2S^2\delta\theta_2 + (8J^2S^2 - H^2)(\delta\theta_1 + \delta\theta_3) &= -2h'_{4s}H_0 \\ 16J^2S^2\delta\theta_3 + (8J^2S^2 - H^2)(\delta\theta_2 + \delta\theta_4) &= -2h_{4s}H_0 \\ 16J^2S^2\delta\theta_4 + (8J^2S^2 - H^2)(\delta\theta_1 + \delta\theta_3) &= 2h'_{4s}H_0 \end{aligned} \quad (\text{S14})$$

Solving Eq. S14 leads to a simple correlation between  $\delta\theta_n$  and the staggered fields that:

$$\begin{aligned} \delta\theta_1 &= \frac{h_{4s}H_0}{8J^2S^2} \\ \delta\theta_2 &= -\frac{h'_{4s}H_0}{8J^2S^2} \\ \delta\theta_3 &= -\frac{h_{4s}H_0}{8J^2S^2} \\ \delta\theta_4 &= \frac{h'_{4s}H_0}{8J^2S^2} \end{aligned} \quad (\text{S15})$$

At this point, it is more convenient to write the staggered field in terms of  $\delta\theta_n$ . Comparing Eq. S15 with Fig. S6, we can get that the staggered field on the  $n$ th site,  $h_n$ , is:

$$h_n = (-1)^{n+1} \frac{8J^2S^2}{H_0} \delta\theta_n. \quad (\text{S16})$$

The effective spin Hamiltonian for Cu(pym) in the laboratory frame ( $XYZ$  in Fig S6) can be written as:

$$\hat{\mathcal{H}} = \sum_n J(\hat{S}_n^X \hat{S}_{n+1}^X + \hat{S}_n^Y \hat{S}_{n+1}^Y + \hat{S}_n^Z \hat{S}_{n+1}^Z) - H_0 \hat{S}_n^X + (-1)^n \frac{8J^2S^2}{H_0} \delta\theta_n \hat{S}_n^Z. \quad (\text{S17})$$

The first term in Eq. S17 represents the antiferromagnetic interactions. The second and third terms are the Zeeman interactions due to the external field  $H_0$  and the staggered fields  $h_n$ , respectively.  $\hat{S}_n^X$ ,  $\hat{S}_n^Y$  and  $\hat{S}_n^Z$  correspond to the spin operators in the laboratory frame. They are related to the spin operators in the rotating frame ( $\hat{S}_n^x$ ,  $\hat{S}_n^y$  and  $\hat{S}_n^z$ ) in the following way:

$$\begin{aligned} \hat{S}_n^X &= (-1)^{(n+1)} \hat{S}_n^x \cos \theta_n + \hat{S}_n^z \sin \theta_n \\ \hat{S}_n^Y &= -\hat{S}_n^y \\ \hat{S}_n^Z &= (-1)^n \hat{S}_n^z \cos \theta_n + \hat{S}_n^x \sin \theta_n \end{aligned} \quad (\text{S18})$$

In the rotating frames, the ground state of the chain corresponds to the  $n$ th spin being parallel to  $z_n$ . By substituting Eq. S18 into Eq. S17 the Hamiltonian in the rotating frame can be written as:

$$\begin{aligned} \hat{\mathcal{H}} &= \sum_n J[-\cos(\theta_n + \theta_{n+1})(\hat{S}_n^x \hat{S}_{n+1}^x + \hat{S}_n^z \hat{S}_{n+1}^z) + \hat{S}_n^y \hat{S}_{n+1}^y + (-1)^{n+1} \sin(\theta_n + \theta_{n+1})(\hat{S}_n^x \hat{S}_{n+1}^z - \hat{S}_n^z \hat{S}_{n+1}^x)] \\ &\quad + H_0[(-1)^n \cos \theta_n \hat{S}_n^x - \sin \theta_n \hat{S}_n^z] \\ &\quad + (-1)^n \frac{8J^2S^2}{H_0} \delta\theta_n [(-1)^n \cos \theta_n \hat{S}_n^z + \sin \theta_n \hat{S}_n^x], \end{aligned} \quad (\text{S19})$$

The spin operators can be written via bosonic operators using the Holstein-Primakoff transformation. The leading order expansion for a spin pointing in the  $z$ -direction is:

$$\begin{aligned} \hat{S}_n^x &= \sqrt{\frac{S}{2}}(a_n^\dagger + a_n) \\ \hat{S}_n^y &= i\sqrt{\frac{S}{2}}(a_n^\dagger - a_n) \\ \hat{S}_n^z &= S - a_n^\dagger a_n \end{aligned} \quad (\text{S20})$$

Substituting Eq. S20 into Eq. S19, the Hamiltonian can be written as  $\hat{\mathcal{H}} = \hat{\mathcal{H}}_0 + \hat{\mathcal{H}}_1 + \hat{\mathcal{H}}_2 + \dots + O(H_0) + O(h_{4s}, h'_{4s})$ .  $\hat{\mathcal{H}}_n = O(S^{2-n/2})$  is the field independent part whereas  $O(H_0)$  and  $O(h_{4s}, h'_{4s})$  correspond to the contributions due to the applied field  $H_0$  and the four-fold staggered fields, respectively. By substituting Eq. S20 into Eq. S19, we get:

$$\begin{aligned}
\hat{\mathcal{H}}_0 &= \sum_n -JS^2 \cos(\theta_n + \theta_{n+1}) \\
\hat{\mathcal{H}}_1 &= \sum_n (-1)^{(n+1)} J \frac{S^{3/2}}{2^{1/2}} [\sin(\theta_{n-1} + \theta_n) + \sin(\theta_n + \theta_{n+1})] (a_n^\dagger + a_n) \\
\hat{\mathcal{H}}_2 &= \sum_n JS [\cos(\theta_n + \theta_{n+1}) + \cos(\theta_{n-1} + \theta_n)] a_n^\dagger a_n \\
&\quad - \frac{JS}{2} [\cos(\theta_n + \theta_{n+1}) + 1] (a_n^\dagger a_{n+1}^\dagger + a_n a_{n+1}) + \frac{JS}{2} [1 - \cos(\theta_n + \theta_{n+1})] (a_n^\dagger a_{n+1} + a_n a_{n+1}^\dagger) \\
O(H_0) &= \sum_n -H_0 \sin \theta_n S + H_0 (-1)^n \cos \theta_n \sqrt{\frac{S}{2}} (a_n^\dagger + a_n) + H_0 \sin \theta_n a_n^\dagger a_n \\
O(h_{4s}, h'_{4s}) &= \sum_n \left[ \frac{8J^2 S^2}{H_0} \delta \theta_n (S - a_n^\dagger a_n) + (-1)^n \sqrt{\frac{S}{2}} \frac{8J^2 S^2}{H_0} \delta \theta_n \sin \theta_n (a_n^\dagger - a_n) \right]
\end{aligned} \tag{S21}$$

Eq. S21 includes the first three leading orders in the exchange interaction part ( $\hat{\mathcal{H}}_0$ ,  $\hat{\mathcal{H}}_1$  and  $\hat{\mathcal{H}}_2$ ) and all orders in  $H_0$ ,  $h_{4s}$  and  $h'_{4s}$ .  $\hat{\mathcal{H}}_0$  is a constant. Taking into account the constraints for canted angles (Eq. S13) and replacing  $\theta_n$  with  $\theta + \delta \theta_n$ , the Hamiltonian can be written as (to the order of  $S$  in spin-wave expansion):

$$\begin{aligned}
\hat{\mathcal{H}} &= \sum_n 2JS \cos 2\theta a_n^\dagger a_n + H_0 \sin \theta a_n^\dagger a_n \\
&\quad - \frac{JS}{2} (1 + \cos 2\theta) (a_n^\dagger a_{n+1}^\dagger + a_n a_{n+1}) + \frac{JS}{2} (1 - \cos 2\theta) (a_n^\dagger a_{n+1} + a_n a_{n+1}^\dagger) \\
&\quad + \frac{JS}{2} \sin 2\theta (\delta \theta_n + \delta \theta_{n+1}) (a_n^\dagger a_{n+1}^\dagger + a_n a_{n+1} + a_n^\dagger a_{n+1} + a_n a_{n+1}^\dagger) - \frac{8J^2 S^2}{H_0} \cos \theta \delta \theta_n a_n^\dagger a_n \\
&\quad + \frac{JS}{4} \cos 2\theta (\delta \theta_n + \delta \theta_{n+1})^2 (a_n^\dagger a_{n+1}^\dagger + a_n a_{n+1} + a_n a_{n+1}^\dagger + a_n^\dagger a_{n+1}) \\
&\quad \left[ \frac{16J^2 S^2 - H_0^2}{H_0^2} \sin \theta \delta \theta_n^2 - \frac{JS}{2} \cos 2\theta (2\delta \theta_n^2 + \delta \theta_{n-1}^2 + \delta \theta_{n+1}^2) \right] a_n^\dagger a_n
\end{aligned} \tag{S22}$$

The first four terms of Eq. S22 correspond to the spin wave expansion for a uniform antiferromagnetic chain in the presence of an external field  $H_0$  without any staggered field. The fifth and sixth terms are the linear contribution of  $h_{4s}$  and/or  $h'_{4s}$  while the remaining two parts are proportional to  $h_{4s}^2$  and/or  $h'_{4s}{}^2$ . By Fourier transforming Eq. S22, it can be found that the fifth and sixth terms vanish because that the values of  $\delta \theta_n$  oscillate between  $\pm h_{4s} H_0 / 8J^2 S^2$  (or  $\pm h'_{4s} H_0 / 8J^2 S^2$ ). Therefore, the Hamiltonian is:

$$\begin{aligned}
\hat{\mathcal{H}} &= \sum_k \left[ 2JS \cos 2\theta + H_0 \sin \theta - \frac{H_0^2 (16J^2 S^2 - 3H_0^2) (h_\alpha^2 + h_\beta^2)}{1024J^5 S^5} \right. \\
&\quad \left. + (JS - JS \cos 2\theta + \frac{H_0^2 (8J^2 S^2 - H_0^2) (h_\alpha^2 + h_\beta^2)}{1024J^5 S^5}) \cos k \right] a_k^\dagger a_k \\
&\quad - \left[ \frac{JS}{2} (1 + \cos 2\theta) - \frac{H_0^2 (8J^2 S^2 - H_0^2) (h_\alpha^2 + h_\beta^2)}{2048J^5 S^5} \right] \cos k (a_k^\dagger a_{-k}^\dagger + a_k a_{-k}).
\end{aligned} \tag{S23}$$

For clarity, we define the following functions:

$$\begin{aligned}
A(k) &= [2JS \cos 2\theta + H_0 \sin \theta - \frac{H_0^2 (16J^2 S^2 - 3H_0^2) (h_\alpha^2 + h_\beta^2)}{1024J^5 S^5} + (JS - JS \cos 2\theta + \frac{H_0^2 (8J^2 S^2 - H_0^2) (h_\alpha^2 + h_\beta^2)}{1024J^5 S^5}) \cos k] \\
B(k) &= [\frac{JS}{2} (1 + \cos 2\theta) - \frac{H_0^2 (8J^2 S^2 - H_0^2) (h_\alpha^2 + h_\beta^2)}{2048J^5 S^5}] \cos k,
\end{aligned} \tag{S24}$$

and  $\hat{\mathcal{H}} = \sum_k A(k)a_k^\dagger a_k - B(k)(a_k^\dagger a_{-k}^\dagger + a_k a_{-k})$ . By performing the following Bogoliubov transformation:

$$\begin{aligned} a_k &= \cosh \psi_k \alpha_k + \sinh \psi_k \alpha_{-k}^\dagger \\ a_{-k}^\dagger &= \sinh \psi_k \alpha_k + \cosh \psi_k \alpha_{-k}^\dagger \end{aligned} \quad (\text{S25})$$

with  $\tanh 2\psi_k = 2B(k)/A(k)$ , the Hamiltonian (Eq. S23) can be diagonalised that:

$$\hat{\mathcal{H}} = \sqrt{A^2(k) - 4B^2(k)} \alpha_k^\dagger \alpha_k. \quad (\text{S26})$$

which gives a single band in the paramagnetic Brillouin zone. We can equivalently fold the dispersion relation into the antiferromagnetic Brillouin zone,  $-\pi/2 < k < \pi/2$ . This gives us two branches with dispersion relations:

$$\begin{aligned} E_\pm = \{ & [2JS \cos 2\theta + H_0 \sin \theta - \frac{(h_{4s}^2 + h_{4s}'^2)H_0^2 \cos 2\theta}{32J^3 S^3} \pm [JS(1 - \cos 2\theta) + \frac{(h_{4s}^2 + h_{4s}'^2)H_0^2 \cos 2\theta}{64J^3 S^3}] \cos k]^2 \\ & - [JS(1 + \cos 2\theta) - \frac{(h_{4s}^2 + h_{4s}'^2)H_0^2 \cos 2\theta}{64J^3 S^3}]^2 \cos^2 k \}^{1/2} \end{aligned} \quad (\text{S27})$$

In the absence of staggered fields,  $E_- = 0$  and Eq. S27 gives the gapless excitation expected for uniform antiferromagnetic chains. Non-zero four-fold staggered fields lead to a excitation gap ( $\Delta$ ) with the magnitude of the gap being:

$$\Delta = \sqrt{\frac{(h_{4s}^2 + h_{4s}'^2)H_0^2}{J^2 S^2} \times \frac{(16J^2 S^2 - H_0^2)(8J^2 S^2 - H_0^2)}{1024J^4 S^4}} \quad (\text{S28})$$

Eq. S28 shows that the excitation gap is proportional to  $\sqrt{(h_{4s}^2 + h_{4s}'^2)H_0^2/J^2 S^2}$ . The staggered fields are much smaller than the applied field  $H_0$  and the antiferromagnetic interactions  $JS$ . Therefore, comparing with the excitation gap in Cu benzoate [S16, S17] ( $\Delta \propto \sqrt{\hbar JS}$ ) calculated with similar spin-wave expansion technique, the gap in Cu(pym) is expected to be much smaller. We note that by taking into account 1D critical fluctuation, the power-law behavior of the gap in Cu benzoate is changed from  $\hbar^{1/2}$  to  $\hbar^{2/3}$ . We expected similar corrections should also be applied to our calculations, modifying the prediction of the field induced gap.

- 
- [S1] S. J. Blundell, *Contemporary Physics* **40**, 175 (1999), 0207699.  
[S2] R. S. Hayano, Y. J. Uemura, J. Imazato, N. Nishida, T. Yamazaki, and R. Kubo, *Physical Review B* **20**, 850 (1979).  
[S3] C. Yasuda, S. Todo, K. Hukushima, F. Alet, M. Keller, M. Troyer, and H. Takayama, *Phys. Rev. Lett.* **94**, 217201 (2005).  
[S4] T. G. Castner and M. S. Seehra, *Physical Review B* **4**, 38 (1971).  
[S5] A. Zorko, D. Arçon, H. van Tol, L. C. Brunel, and H. Kageyama, *Physical Review B* **69**, 174420 (2004), 0311079.  
[S6] M. Herak, A. Zorko, D. Arçon, A. Potočnik, M. Klanjšek, J. van Tol, A. Ozarowski, and H. Berger, *Physical Review B* **84**, 184436 (2011), 1109.5597.  
[S7] S. J. Balian, G. Wolfowicz, J. J. L. Morton, and T. S. Monteiro, *Physical Review B* **89**, 045403 (2014), 1302.1709.  
[S8] M. Shiddiq, D. Komijani, Y. Duan, A. Gaita-Ariño, E. Coronado, and S. Hill, *Nature* **531**, 348 (2016).  
[S9] S. A. Zvyagin, A. K. Kolezhuk, J. Krzystek, and R. Feyerherm, *Physical Review Letters* **93**, 027201 (2004), 0403364 [cond-mat].  
[S10] F. H. L. Essler, A. Furusaki, and T. Hikihara, *Physical Review B* **68**, 064410 (2003), 0304244 [cond-mat].  
[S11] K. Y. Povarov, A. I. Smirnov, O. A. Starykh, S. V. Petrov, and A. Y. Shapiro, *Phys. Rev. Lett.* **107**, 37204 (2011).  
[S12] A. I. Smirnov, T. A. Soldatov, K. Y. Povarov, M. Hälgl, W. E. A. Lorenz, and A. Zheludev, *Physical Review B* **92**, 134417 (2015), 1507.07518.  
[S13] S. A. Zvyagin, *Low Temperature Physics* **38**, 819 (2012).  
[S14] K. An, T. Sakakibara, R. Settai, Y. Onuki, M. Hiragi, M. Ichioka, and K. Machida, *Physical Review Letters* **104**, 1 (2010), 0911.3443.  
[S15] P. A. Goddard, J. Singleton, P. Sengupta, R. D. McDonald, T. Lancaster, S. J. Blundell, F. L. Pratt, S. Cox, N. Harrison, J. L. Manson, H. I. Southerland, and J. A. Schlueter, *New Journal of Physics* **10**, 083025 (2008).  
[S16] M. Oshikawa and I. Affleck, *Phys. Rev. Lett.* **79**, 2883 (1997).  
[S17] I. Affleck and M. Oshikawa, *Phys. Rev. B* **60**, 1038 (1999).